Electromagnetic Resonance Modification Technique for Optimization of Polarization Conversion Performance in Metastructures

Yu-Peng Li, Zhen Qiao, Ke Xia, Lei Zhang, and Hai-Feng Zhang

***Abstract*— Electromagnetic resonance modification (EMRM) is a promising method for upgrading and optimizing metastructures (MSs) that convert polarization states. The present study offers comprehensive theoretical work to demonstrate that appropriate hole columns and slit structures can be effectively employed to improve the performance of polarization conversion MS, which, in turn, enhances polarization conversion rate (PCR) in defective bands. The variation of PCR at each step is calculated and investigated through the usage of reflection amplitude and phase; furthermore, the inferior resonant frequencies (IRFs) are discussed in detail. The equivalent circuit model and nonlinear coupling mode theory are used to systematically summarize the implementation mechanism of EMRM technology. We observe that the EMRM technique is capable of inducing and re-exciting the directivity, density, and intensity of the surface currents, which is supported by the electromagnetic (EM) field energy distribution. Our findings not only shed light on the operating mechanism of EMRM technology but also offer new avenues for designing ultrawideband and highly efficient polarization conversion MSs.**

***Index Terms*— Electromagnetic resonance modification (EMRM), metastructure (MS), performance optimization, polarization conversion.**

I. Introduction

THE electromagnetic (EM) wave is a fundamental carrier of information in modern science and technology, with wide-ranging development and application prospects in fields such as information communication [1], sensing [2], and national defense security [3]. The Terahertz (THz) wave, which occupies the EM spectrum between microwave and infrared frequencies [4], is defined by its basic properties of amplitude, phase, frequency, and polarization, which determine its propagation state. Among these properties, the polarization state of THz waves is of particular importance, as it carries valuable information in sensitive measurement and signal transmission applications [5]. As such, polarization manipulation techniques are frequently employed in modulators and switches and have been practically applied in a variety of fields such as sensing, imaging, and communication [6], [7], [8]. It is imperative to control the polarization state of THz waves comprehensively, and the development of polarization converters represents an essential step toward achieving this goal.

In accordance with Maxwell's equations, the propagation behavior of EM waves is reliant upon the dielectric constant and permeability of the medium through which they propagate [8]. The ability of natural materials to control EM waves is, however, restricted by their narrow range of permittivity [9], [10]; furthermore, natural materials that lack magnetic response exhibit imperfect impedance match with the environment, which also impairs the polarization conversion of EM waves [11]. These limitations have significantly impeded the progress of device miniaturization and integration, hindering the achievement of high efficiency and compatibility in practical applications. Nonetheless, metastructures (MSs) have overcome these barriers as a significant branch of metamaterials.

The introduction of an artificial structure possessing a negative refractive index and negative dielectric constant by Smith et al. [12], based on Pendry's research [13] opened the door to MSs. Currently, MSs have been extensively studied and verified in various fields, including superlens [14] and EM stealth cloak [15], which offer a new direction for polarization conversion. Jones matrix [16], equivalent circuit [17], Stokes vector [18], Fabry-Perot cavity [19], and multiple interference theories [20] are commonly used to investigate polarization conversion MSs. Numerical simulations are achieved through the finite difference time domain method [21], finite element method [22], and finite integral technique [23]. In the early stages, polarization conversion MSs were primarily focused on single or multifrequency operations. With ongoing design improvements, the continuous working band is becoming increasingly attainable. At present, efficient and stable polarization conversion throughout the ultrawideband is the primary design goal and quality requirement for polarization conversion MSs.

Recent research has highlighted the constructive role of hole columns in inducing and limiting EM fields. For instance, Maccaferri et al. [24] explored a 2-D plasmonic crystal containing a periodic array of cylindrical holes in a ferromagnetic layer. They discovered that specific conditions could lead to resonance enhancement of the magneto-optical response in the

Manuscript received 19 April 2023; revised 9 July 2023; accepted 29 July 2023. Date of publication 9 August 2023; date of current version 6 October 2023. This work was supported by the Postgraduate Research and Practice Innovation Program of Jiangsu Province under Grant KYCX22_0931. *(Corresponding author: Hai-Feng Zhang.)*

The authors are with the College of Electronic and Optical Engineering and the College of Flexible Electronics (Future Technology), Nanjing University of Posts and Telecommunications, Nanjing 210023, China (e-mail: hanlor@163.com).

This article has supplementary material provided by the authors and color versions of one or more figures available at https://doi.org/10.1109/TAP.2023.3302028.

Digital Object Identifier 10.1109/TAP.2023.3302028

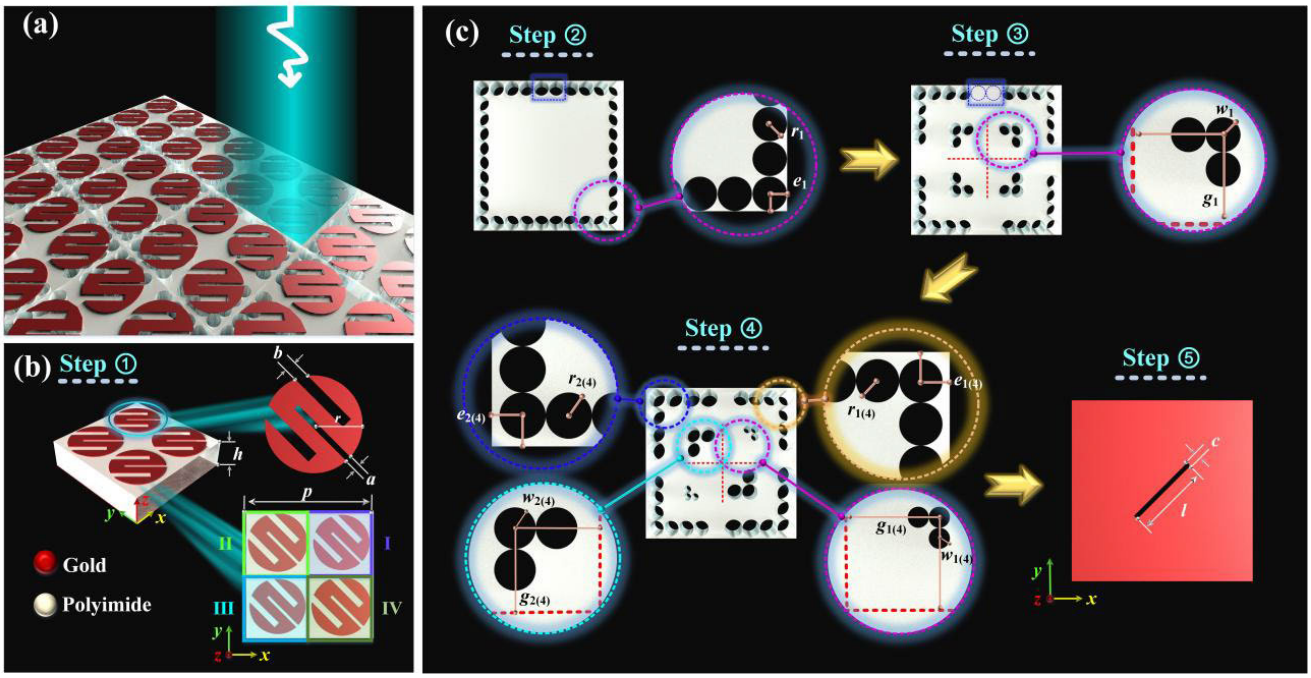

Fig. 1. Schematic of the proposed MS and the implementation details of EMRM technology. (a) Periodic array of MS. (b) Initial lattice unit called Step ①. (c) Structural changes implemented by EMRM technology in the process of optimizing lattice units.

longitudinal Kerr configuration. In another study, Wang and Wu [25] designed a cavity-based linear-to-circular polarization converter in which the hole columns affect mode excitation and field limitation. When aiming to design a multitasking device with switchable and tailored functions of ultrabroadband absorption and polarization conversion, Zhang et al. [26] suggested that constructing a cylindrical gas column could provide an effective channel for broadening the absorption bandwidth. Additionally, designing the hole column as the substrate-integrated waveguide could stimulate more applications through the resonant mode of the cavity, as demonstrated in Zhu et al. [27], where the cross-polarization reflection coefficient zero is caused by the coupling effect of two degenerate modes in the substrate-integrated waveguide cavity. In another study, Amiri et al. [28] used a perfect metamaterial absorber based on a hole column cavity to remotely sense soil moisture. High-resolution sensing was achieved by creating physical channels in the substrate-integrated waveguide cavity; however, the systematic development and demonstration of using such structures to enhance polarization conversion performance (including amplitude adjustment, phase matching correction, polarization conversion rate (PCR) enhancement, and working band expansion) is yet to be achieved. Further investigation and experimentation are, therefore, necessary to determine the full potential of hole columns in promoting efficient and effective polarization conversion.

In this article, we present an EM resonance modification (EMRM) technique for enhancing the performance of polarization conversion MS. By using hole columns, we explore methods to improve the inferior resonance frequencies (IRFs) of these structures. Our stepwise optimization process of defect MSs highlights the contribution of the EMRM technology to amplitude adjustment and phase matching, as well as its significant effect in improving the polarization conversion ratio and expanding the operating band. The EMRM technology is based on the guided polarization conversion effect, which employs hole columns to induce and enhance currents in the metal reflector, and uses a slit structure as an auxiliary for surface current excitation. Effective resonant currents form the basis of EM resonance, which supports the polarization conversion effect. With the EMRM technology, we demonstrate that the operating band with internal depression (PCR < 0.9) can be made continuous and stable. The example MS presented in this article improves the PCR while indirectly expanding the operating band, achieving the goals of enhancing and optimizing polarization performance. Our work not only systematically demonstrates the reliability of the EMRM technology but also provides an ultrawideband MS with high efficiency for polarization conversion. This technology and MS have broad application prospects in the design of radomes, optical switches, and other related fields.

II. Structural Design and Results of MS Unit

The potential of MS in reflective polarization conversion by integrating a designed lattice unit periodically along the x- and y-axes is explored, as shown in Fig. 1(a). Our focus is on investigating the implementation of the EMRM technology, and hence the designed resonant structures serve only as key configurations that aid in revealing the underlying physical principles and as an intuitive application example. The original configuration studied in this work is a 2×2 lattice unit composed of a traditional metal reflector, dielectric substrate, and resonant metal patch, as shown in Fig. 1(b). Specifically, the lattice unit is viewed as four quadrants [i.e., quadrants I–IV in Fig. 1(b)]. The metal resonator in quadrant I is composed of circular patches with a radius of r arranged in a staggered

slit pattern, while quadrant III is identical to quadrant I. Quadrant II, which is congruent to quadrant IV, is obtained by scaling up quadrant I by a factor of k. The overall original lattice unit (referred to as Step ①) exhibits axis symmetry along the u-axis. The metal structure employs gold with a conductivity of 4.561×10^7 S/m [29] and a thickness of 0.2 μm. The dielectric substrate has a side length of p and a thickness of h and is made of Polyimide (lossy) with a relative dielectric constant of 3.5 and a loss tangent of 0.008 [30].

The present study investigates the optimization effect of EMRM technology on performance. The optimization of the system structure is primarily demonstrated through the implementation of hole-column technology (Step ②∼④) and slit technology (referred to as Step ⑤). The system's scanning image is presented in Fig. 1(c). The study first uses specially designed subwavelength air hole columns, which are arranged continuously in a square lattice dielectric substrate, and the hole column's depth is consistent with the dielectric substrate's thickness. Step ② optimizes Step ① through the implementation of hole-column technology, where the hole-columns with radius r_1 are positioned at a distance (e_1) from the edge of the dielectric substrate. The hole columns of identical size and specification are independently arranged along the x- and y-axis in lattice units, forming a continuously closed "hole-column frame" at the outer edge of the dielectric substrate. In Step ③, the two holes on each side of the "hole-column frame" are filled, as indicated by the blue dotted line, converting the closed "hole-column frame" into the outer "hole-column corner" in each of the four quadrants. Furthermore, in Step ③, the fresh hole columns with radius w_1 are positioned at g_1 from the center quadrant dividing line, extending to form an inside "hole-column corner" in the same direction as the outside one. Currently, the hole columns in the lattice unit dielectric substrate are center symmetric. In Step ④, the radius and the positioning of the hole columns have changed. Due to the symmetry of metal resonant structures, the hole columns' variation follows the principle that quadrants I, III, and II, IV remain unified, respectively.

In addition to modifying the hole columns, the implementation of EMRM technology can also be achieved through the slit structure, as denoted in Step ⑤. Specifically, the hole columns from Step ④ are maintained, and a slit is etched in the metal reflector extending along the v-axis. This completes the second part of the EMRM technique in the structural design process. The modeling process and simulation analyses mainly rely on HFSS, a 3-D EM simulation software. The vertically incident EM waves are emitted from the Floquet port installed at the top of the unit, and the boundary conditions are set to primary-secondary mode. The lattice cells' structural parameters are detailed in Table I.

Assuming that the polarization direction of the incident wave is aligned with the y-axis. In a 2-D coordinate system, the physical quantities located on the x- and y-axes are decomposed in a 45° direction, resulting in components along the u- and v-axes, as shown in Fig. 2. In resonant structures, the u- and v-axes generally exhibit mirror symmetry, allowing us to neglect the values of r_{mn} and r_{nm}. Here, r_{mn} refers to the reflection coefficient of the EMW with polarization direction

TABLE I
RELEVANT PARAMETERS AND VALUES INVOLVED IN THE IMPLEMENTATION OF EMRM TECHNOLOGY

Parameter	b	r	a	h	p
Value (μm)	6	26	3	30	120
Parameter	r_1	e_1	w_1	g_1	$e_{2(4)}$
Value (μm)	6	6	5	25	8
Parameter	$r_{2(4)}$	$r_{1(4)}$	$e_{1(4)}$	$w_{2(4)}$	$g_{2(4)}$
Value (μm)	7	6	8	6	23
Parameter	$g_{1(4)}$	$w_{1(4)}$	c	l	k
Value (μm)	27	3	3	50	0.06

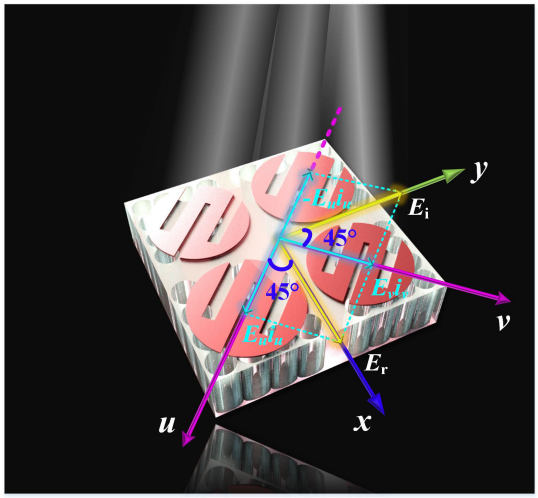

Fig. 2. Schematic of EM wave decomposition.

from n to m, and similar methods can be used to define other physical quantities. To achieve the optimal polarization conversion performance, certain conditions need to be satisfied: $|r_{uu}| = |r_{vv}| = 1$ and the phase difference $\Delta\varphi = \varphi_{vv} - \varphi_{uu} = \pi \pm 2n\pi$. The polarization conversion ratio is a widely accepted metric for evaluating the effectiveness of reflective polarization conversion MSs. It is defined using the reflection amplitude coefficients as $\mathrm{PCR} = r_{xy}^2/(r_{xy}^2 + r_{yy}^2)$. In the absence of energy loss, due to energy conservation, $r_{xy}^2 + r_{yy}^2 = 1$ can be obtained; therefore, $\mathrm{PCR} = 1 - r_{yy}^2$. It is generally considered that $\mathrm{PCR} \geq 0.9$ meets the design target, which corresponds to a copolarized reflection coefficient $|r_{yy}| \leq -10$ dB. To satisfy this criterion, the derived phase conditions are $\pi - 37° \leq |\Delta\varphi| \leq \pi + 37°$ [31].

It is important to emphasize that the basic design concept of the original configuration is based on the principles mentioned above. Resonance conditions of EMWs in quadrant I, and quadrant II, as well as within the 2×2 lattice unit, can be obtained through simulations and characterized using PCR. Fig. 3(a) illustrates the PCR in quadrant I, where polarization conversion takes place within the range of 0.64–1.32 THz (although the PCR values are relatively high, they do not meet the requirement of values exceeding 90% continuously); however, the resonance at 1.22 THz, represented by the IRF

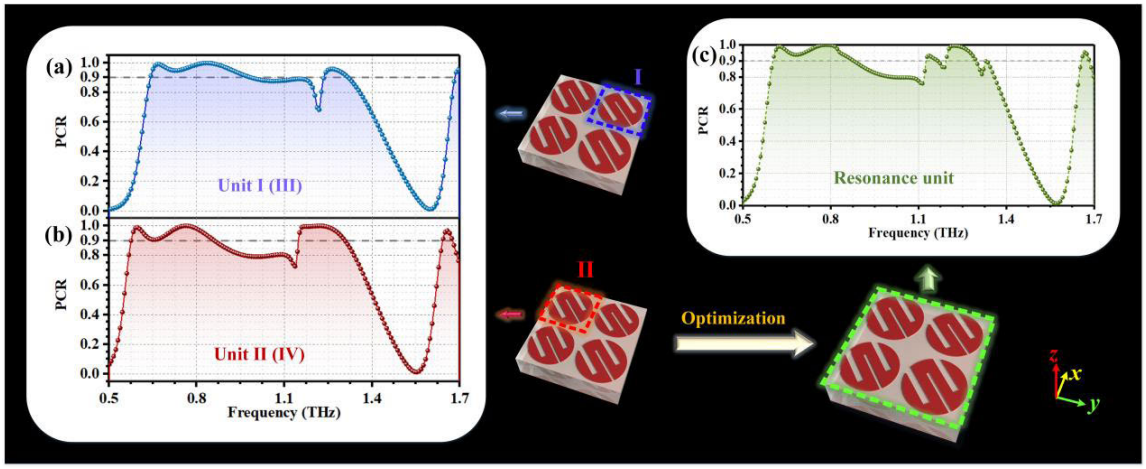

Fig. 3. Quadrant structures performance (PCR) description. (a) Quadrant I (III). (b) Quadrant II (IV). (c) Original lattice unit.

(PCR $\leq$ 0.9), is insufficient, resulting in a lower PCR value of 0.68. Quadrant II's resonant patch is obtained by scaling up quadrant I by k times, causing a redshift, while the trend of the PCR curve remains similar. The range of the polarization conversion effect extends from 0.58 to 1.30 THz, and the IRF is located at 1.13 THz (PCR = 0.72). The detrimental impact on the mid-frequency by the IRF intensifies, as depicted in Fig. 3(b).

A unit lattice of size 2 × 2 is composed of the two aforementioned structures, whose PCR curve is depicted in Fig. 3(c). The 2 × 2 combination mode moderately broadens the bandwidth of the polarization conversion effect (0.60∼1.33 THz), reproducing and superimposing the particular resonant frequencies generated in each quadrant. Three IRFs are presently awaiting optimization at high frequencies, specifically at 1.11, 1.19, and 1.32 THz. Simultaneously, the performance shortcomings at the intermediate frequency range require further optimization. We would like to emphasize that this article's primary focus is on discussing the universal optimization effects of EMRM technology on polarization conversion MSs. The lattice unit configuration is of paramount importance in revealing the underlying principles and serves as a potential application case. A broader operating band would, therefore, make the optimized MS suitable for more extensive applications; furthermore, the continuous appearance of IRFs reveals more possibilities for applying EMRM technology, thereby making the performance tuning process more convincing.

To summarize, the IRFs located at frequencies of 1.11, 1.19, and 1.32 THz in Step ① are depicted in the PCR curve shown in Fig. 4(b_1). In Fig. 4(a_1), the cross-polarized reflection amplitude (r_{yx}) curve reveals that the above IRFs have cross-polarized reflection amplitudes lower than 0.8 due to insufficient resonance at these frequencies. The IRF at 1.11 THz induces the copolarized reflection amplitude (r_{yy}) in the intermediate band to reach 0.43. The slight difference between the reflection amplitudes of cross-polarized and copolarized waves indicates that only a portion of the incident y-polarized EM wave is transformed into the required x-polarized wave under the influence of the MS; furthermore, a significant proportion of y-polarized EM waves accompany the emission, resulting in a hybrid outgoing wave that adversely affects the device's performance. As a result, the severe resonant defects in the intermediate frequency become the primary difficulty to overcome. In Step ②, EMRM technology is employed to significantly decrease the excessive copolarized reflection amplitude at the intermediate frequency. The r_{yy} is stabilized below 0.2 in the 0.90∼1.31 THz range and even as low as 0.01 at 1.00 THz, as displayed in Fig. 4(a_2). The "hole-column frame" can be interpreted as reducing the effective electric dimension of the lattice unit to some extent. The band with the polarization conversion effect, therefore, slightly blue-shifts to about 0.70∼1.50 THz. At the same time, the IRFs in Step ① relocate to 1.13, 1.32, and 1.49 THz. The resonance at 1.13 THz satisfies the requirement of PCR $\geq$ 90% in the process of optimizing the intermediate frequency.

Nevertheless, the alterations in the structure during Step ② have negative effects on both low and high frequencies to varying degrees, which are remedied in Step ③, as evidenced by Fig. 4(a_3) and (b_3). Notably, the 1.49 THz IRF's PCR increased by 16%. The PCR at low frequency also met the standard. Furthermore, the PCR is further enhanced at low frequencies during Step ④. The remaining IRFs in Step ③ (located at 1.34 and 1.49 THz) are also significantly optimized in Step ④. Specifically, the PCR at 1.34 THz reached 96.4%, which is negligible, as shown in Fig. 4(b_3). Although the IRF that moved from 1.49 to 1.52 THz still exists, the PCR is increased to 0.86 by numerical calculation, owing to the considerable improvement in r_{yx} (up to 0.87).

Fig. 4(a_5) and (b_5) demonstrate that the IRFs mentioned above are ultimately improved in Step ⑤, and PCR is stabilized above 0.9 in the 0.70∼1.52 THz range, all thanks to the EMRM technique. Notably, the slit structure in Step ⑤ does not consume excessive EM waves, and the total amplitude of the reflected EM wave remains high, especially for the cross-polarized reflection wave. For the reflective MS, the slit on the metal reflector shifts from destructive to constructive. Further detailed specifications of the optimization process are summarized in Table II.

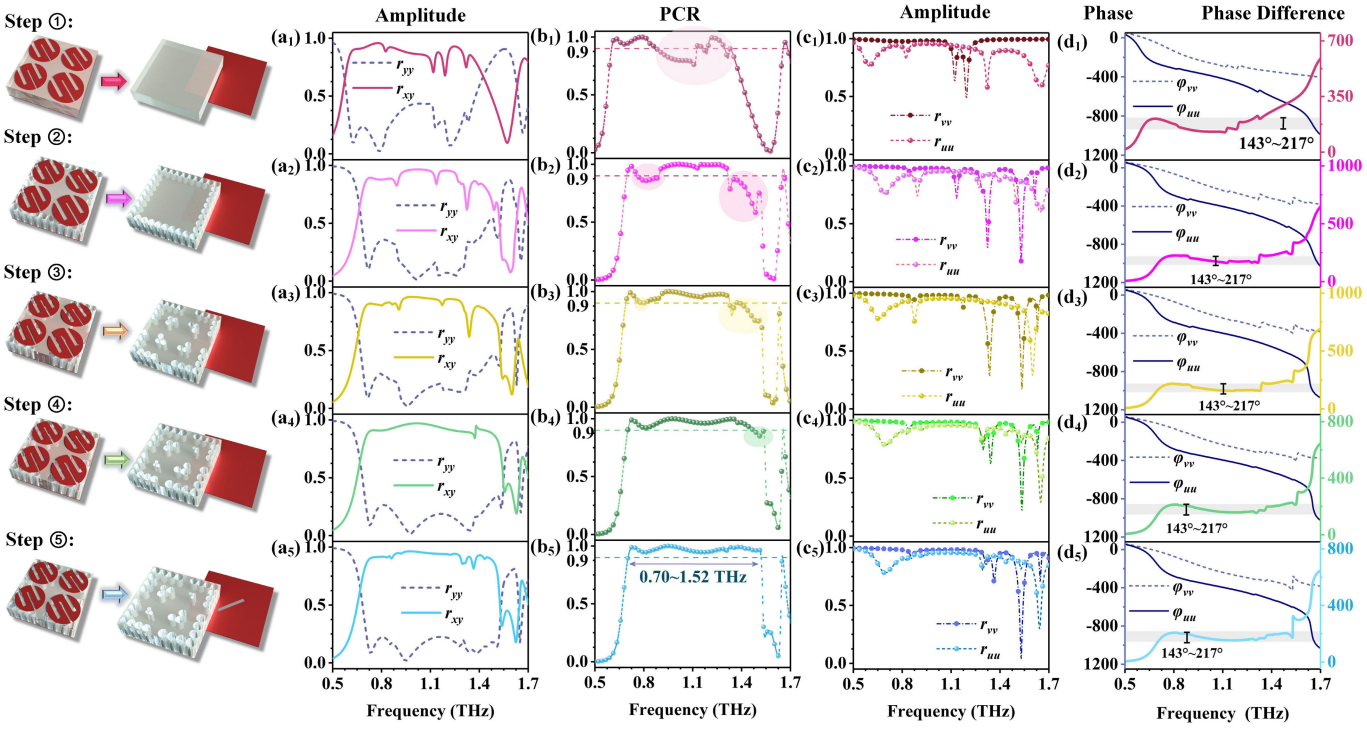

Fig. 4. Curves variation of performance indexes in the optimization process of EMRM technology for the MS from Step ① to Step ⑤. (a_1)–(a_5) Copolarized reflection coefficients (r_{yy}) and the cross-polarized reflection coefficients (r_{xy}). (b_1)–(b_5) PCR. (c_1)–(c_5) Copolarized reflection coefficients of EM wave decomposed into u-axis and v-axis (i.e., r_{uu} and r_{vv}). (d_1)–(d_5) Corresponding phase amplitudes and phase differences.

TABLE II
CHANGES IN IRFS DURING THE OPTIMIZATION PROCESS USING EMRM TECHNOLOGY

Structure	Existing IRF(s)	Optimization IRF(s)	Operating Band (PCR>0.9)	Relative bandwidth
Step ①	1.11 THz	\	0.60~0.87 THz	36.7%
	1.19 THz		1.12~1.16 THz	3.5%
	1.32 THz		1.19~1.29 THz	7.2%
Step ②	0.80 THz	1.13 THz (i.e. 1.11 THz in Step ①)	0.70~0.76 THz	8.2%
	1.32 THz		0.89~1.31 THz	38.2%
	1.49 THz			
Step ③	1.34 THz	1.49 THz	0.70~1.33 THz	62.1%
	1.49 THz			
Step ④	1.52 THz	1.34 THz	0.70~1.47 THz	70.9%
Step ⑤	\	1.52 THz	0.70~1.52 THz	73.9%%

Generally, the physical quantities r_{uu} and r_{vv} are considered to have equivalent values that tend toward 1, as reflected in the stepwise optimization of the MS. Fig. 4(c_1)–(d_5) provide a detailed explanation of the changes in r_{uu}, r_{vv}, and the phase difference when the polarization direction of the outgoing EM wave is decomposed along the u- and v-axes. In Step ①, r_{vv} displays values of 0.62 and 0.48 at 1.11 and 1.19 THz, respectively, which deviates significantly from the expected value. Likewise, r_{uu} also shows the same situation at 1.32 THz, consistent with the IRFs in the PCR curves. Gradual improvement by the EMRM technology corrects the deviation between r_{uu} and r_{vv}. The trend displayed in Fig. 4(c_1)–(c_5) is generally consistent with that in Fig. 4(a_1)–(a_5), rendering further details unnecessary. Ultimately, Fig. 4(c_5) illustrates that r_{uu} and r_{vv} fit each other and are close to 1 in the range of 0.77∼1.33 THz. In the range of 0.70∼1.52 THz, the deviation is relatively weak and acceptable. A deviation analysis of the results is conducted, and several conclusions are drawn. First, the PCR is not a perfect fit to 100%, making deviation from the actual results inevitable. Second, for simplicity, the resonant structure is assumed to be mirror-symmetric on both u- and v-axes during equation derivation, resulting in the assumption

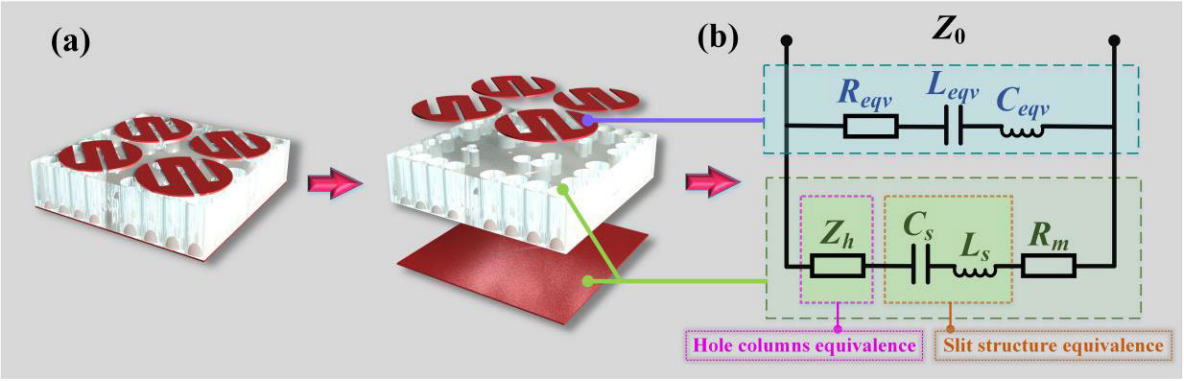

Fig. 5. (a) Structural diagram of the MS lattice unit, and (b) its corresponding equivalent circuit model.

that r_{uv} and r_{vu} are 0 [32]. The proposed resonant structure is, however, not entirely mirror-symmetric, leading to some deviation. Finally, the equation derivation is based on lossless conditions. In the simulation, the metal's ohmic loss and the dielectric substrate's loss tangent are both crucial factors that generate deviation [33].

In fact, the evaluation of polarization conversion MS requires a comprehensive process rather than relying solely on an independent index. Combining and analyzing the reflection amplitude and phase difference is, therefore, necessary. Fig. 4(d_1)–(d_5) provide detailed records of the phase and phase difference for Step ①∼⑤. Within the interval of 0.60∼1.29 THz, Step ① displays a continuous frequency band (0.89∼1.13 THz) that does not conform to the phase condition. The phase difference at 1.11 THz is 124°, which is the most significant deviation from the target range. In Fig. 4(d_2), the phase difference at intermediate frequencies tends to stabilize, while the phase difference at high frequencies mismatches at 1.34 and 1.52 THz due to φ_{vv} jitter. This finding is consistent with the previous description of the reflection amplitude and PCR. The above findings indicate that the physical quantities of IRFs with insufficient resonance maintain a consistent variation trend. Step ④ improves the phase jitter of φ_{vv} at 1.34 THz. In Step ⑤, the phase difference rapidly increases from the value approaching zero and stabilizes between 143° and 217° in the range of 0.70∼1.52 THz, realizing phase matching. Without changing the resonant patches that the lattice units have, it can be observed that the EMRM technology gradually optimizes IRFs and successfully improves the defect of inadequate resonance.

The effective usage of EMRM technology in enhancing the polarization conversion performance hinges on localized modification of the EM wave response within the MS. To this end, an equivalent circuit model is established to elucidate the significant role of EMRM technology in the current local reset. As previously described and depicted in Fig. 5(a), the MS consists of metal resonant patches, a dielectric substrate, and a metal reflective plate arranged in a vertical stack. For the 2 × 2 circular metal patches with slits, the slit capacitance and coplanar capacitance between the patches are collectively represented as C_{eqv}, while the self-inductance arising from the metal resonant patches is denoted by L_{eqv}. The resistance R_{eqv} accounts for both the ohmic and radiation losses of the metal resonant patches. Given that the proposed lattice unit is a mere demonstrative carrier of EMRM technology, the circuit of the metal resonant patches is not comprehensively detailed but instead represented as a general *RLC* series circuit for illustrative purposes, where the equivalent inductance L_{eqv} and equivalent capacitance C_{eqv} are expressed using (1) [34]. The finite difference time domain method enables the computation of the stored electric energy W_{e}, magnetic energy W_{m}, and corresponding current

$$L_{\text{eqv}} = \frac{W_{\text{m}}}{|I_L|^2}, \quad C_{\text{eqv}} = \frac{|I_C|^2}{2\omega W_{\text{e}}}. \tag{1}$$

The usage of equivalent circuit models enables a comprehensive understanding of the functionality and characteristics of hole column and slit structures. In Fig. 5(b), a parallel circuit composed of equivalent resistance (R_{eq}), equivalent inductance (L_{eq}), and equivalent capacitance (C_{eq}) is considered, which typically corresponds to the combination of a dielectric substrate and a metal reflector, with R_{m} representing the loss in the metal reflector. Because of material limitations, hole columns fail to generate sufficient current during EMW resonance, rendering them devoid of inductance and capacitance attributes. By analogizing the characteristic impedance of hole column structures in equivalent acoustic circuit models [35], [36], we can simulate their characteristic impedance in EM media.

Equations (2)–(4) illustrate that the crucial parameters governing the impedance characteristics of hole columns include the radius (r) and depth (d) of the columns, the porosity (p) of the perforated plate, the cross-sectional area (S) of the hole-column structures, the number of columns (n), and the speed of EMW ($c = 3 \times 10^8$ m/s). The impedance of the pore columns ($Z_{\text{h}} = X_{\text{h}} + jY_{\text{h}}$) can be estimated, where X_{h} represents the resistance, and Y_{h} represents the reactance, based on these parameters. By projecting the impedance characteristics onto the metal reflector, we can simulate the influence of hole columns on current redistribution. The flexibility in adjusting the position, radius, and quantity of the hole columns enables precise control of the local impedance of the metal reflector. From the aforementioned equations, it can be inferred that the radius and quantity of the hole columns can alter the impedance values, corresponding to the extent of additional impact exerted by the hole columns on the metal reflector.

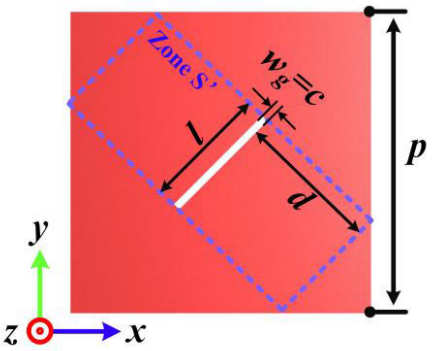

Fig. 6. Structural schematic of the metal reflective plate with a slit structure.

The positioning of the hole columns can modify the range of influence on the metal reflector. Regional variations in the additional local impedance serve to locally excite and guide the current, highlighting their crucial significance in the employment of hole columns within EMRM technology

$$X_{\mathrm{h}} = \frac{8\mu t}{pcr^2}\left(\sqrt{1+\frac{k^2}{32}}+\frac{\sqrt{2}\,kr}{16t}\right) \tag{2}$$

$$Y_{\mathrm{h}} = \frac{\omega t}{pc}\left(1+\frac{1}{\sqrt{9+\frac{k^2}{2}}}+0.85\frac{r}{2t}\right) \tag{3}$$

$$k = \frac{r}{4}\sqrt{\frac{\omega}{t}}, \quad p = \frac{n\pi r^2}{S}. \tag{4}$$

The introduction of a slit structure on the metal reflective plate generates additional capacitance Cs and inductance Ls, as illustrated in Fig. 5(b). The lumped capacitance and inductance of the banded grid can be calculated using (5) and (6) based on transmission line theory [37], where d represents the width of the metal strip, w_{g} is the width of the slit, $\varepsilon_{\mathrm{eff}}$ is the average dielectric constant of the air and dielectric substrate on both sides, and μ_0 is the permeability of the vacuum. Fig. 6 demonstrates the application of this theory to metal reflective plates, where the region S' is treated as a banded grid with a single gap, and w_{g} is equivalent to c, $d = (\sqrt{2}p - l - c/2)$. As evidenced by the equations, the slit width w_{g} and metal strip width d influence the lumped capacitance and inductance, and the latter is determined by the slit length l and width c; therefore, l and c become crucial parameters for the value of capacitance and inductance. In the context of the EMRM technique, the additional capacitance Cs and inductance Ls induced by the slit structure on the metal reflective plate can stimulate a strong resonant current, which plays a positive and constructive role in improving the polarization conversion performance. Furthermore, the hole columns and slit structure help adjust the impedance of the MS, which, in turn, enhances the impedance matching between the device and the air

$$Cs \approx 4\frac{\varepsilon_{eff}\left(w_g+d\right)}{2\pi}\boldsymbol{ln}\frac{\left(w_g+d\right)}{\pi w_g} \tag{5}$$

$$Ls \approx \frac{\mu_0\left(w_g+d\right)}{2\pi}\boldsymbol{ln}\frac{2\left(w_g+d\right)}{\pi d} \tag{6}$$

$$I_{SHG} \propto \left[\frac{2\omega^2\chi_a^{(2)}}{\varepsilon_0 c^2}\right]^2\left|\frac{\sin\left(\frac{\Delta kh}{2}\right)}{\frac{k_{2,0}\Delta k}{2}}\right|^2|A_0|^4|\Xi|^2 e^{-2k_{2,0}^i h} \times \iint_{rect}\mathrm{dxdy}\left|\boldsymbol{E}_{2,0}(x,y)\right|^2 \tag{7}$$

$$\Xi = \frac{\iint_S\left(\boldsymbol{E}_{1,0}\boldsymbol{E}_{1,0}\right):\boldsymbol{E}_{2,0}^*\mathrm{dxdy}}{\iint_S\left|\boldsymbol{E}_{2,0}\right|^2\mathrm{dxdy}}. \tag{8}$$

The nonlinear coupled mode theory is used to comprehend the EMRM technology in addition to constructing an equivalent circuit. The hole columns significantly amplify the intensity of the second harmonic component in the EM wave [38]. This phenomenon is discernible from the electric field obtained through the 3-D finite-difference time-domain method. Fig. 7(a)–(c) depict the electric field distribution of the dielectric substrate with hole columns (front view at $z = h/2$ and side view) when the lattice unit of Step ②∼Step ④ lacks the metal resonant patches and reflective plate. For the y-polarized electric field, the inside of the hole columns manifests strong convergence effects along the y-axis. Particularly, the electric field intensity inside the longitudinal hole columns reaches up to 1.7×10^5 V/m, which significantly surpasses that in the surrounding area. (It should be noted that the values provided in this paragraph, as well as in subsequent descriptions of this article, pertaining to the electric field and magnetic field intensity, represent absolute values.) Observing the side view of the electric field reveals that the intensity of the second harmonic gradually increases from the incident plane to the outgoing one.

The intensity of the second harmonic detected at the exit port can be expressed by (7), according to [39]. The quantum overlap factors Ξ are defined by (8), where $k_{2,0}$ represents the complex propagation wave vector, $\chi_{\mathrm{a}}^{(2)}$ denotes the nonlinear susceptibility, and Δk denotes the phase mismatch between the fundamental wave and the second harmonic waveguide mode. S is the surface area of the inner wall of the hole column. $\boldsymbol{E}_{2,0}(x,y)$ represents the dimensionless transverse mode distribution of the second harmonic waveguide mode, and $\boldsymbol{E}_{2,0}^*(x,y)$ depicts the transverse mode function. The enhancement effect of the second harmonic inside the hole columns provides an opportunity to improve the polarization conversion performance. In the presence of the metal resonant patches and reflective plate, the EM wave resonates between them, and the second harmonic, whose intensity is amplified in the hole columns, repeatedly reinforces the resonance state in a specific region during the polarization conversion process; therefore, the enhancement effect of the second harmonic inside the hole columns drives the precise resonance strengthening in the local area.

Fig. 8 provides a clear and concise depiction of the general implementation process of the EMRM technique, serving as evidence for the universality of this optimization method. In this flowchart, the symbol "Y" represents a positive judgment result ("yes"), while "N" represents a negative judgment result ("no"). The complete optimization process of the MS (from Step ① to Step ⑤), serving as the illustrative carrier in this article, is annotated in the flowchart for better comprehension. To optimize any polarization conversion MS

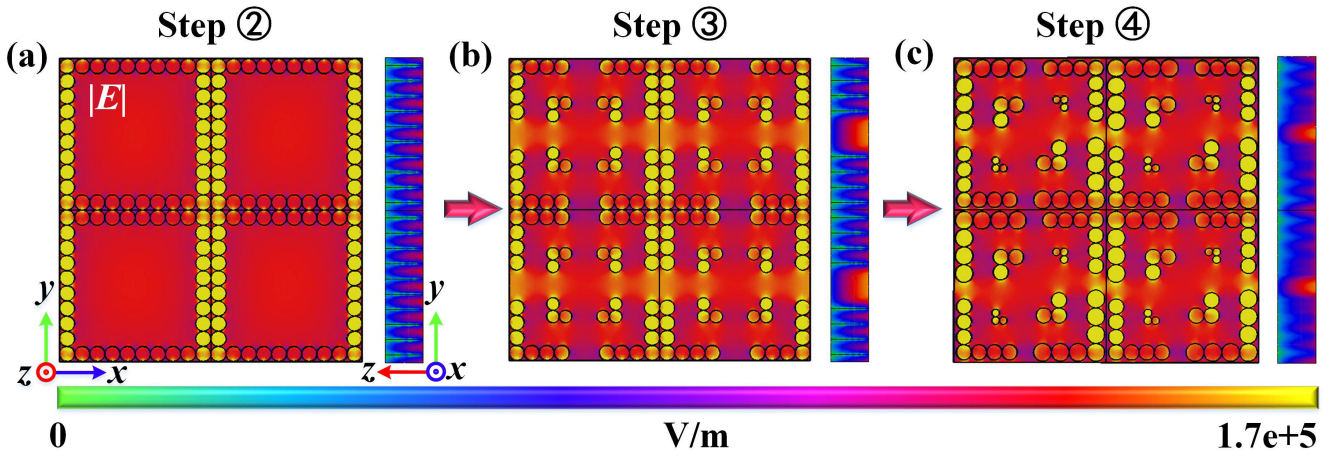

Fig. 7. Electric field distribution of the dielectric substrate with hole columns without metal resonant patches and reflective plate for a lattice unit (front view at $z = h/2$ and side view) in (a) Step ②, (b) Step ③, and (c) Step ④.

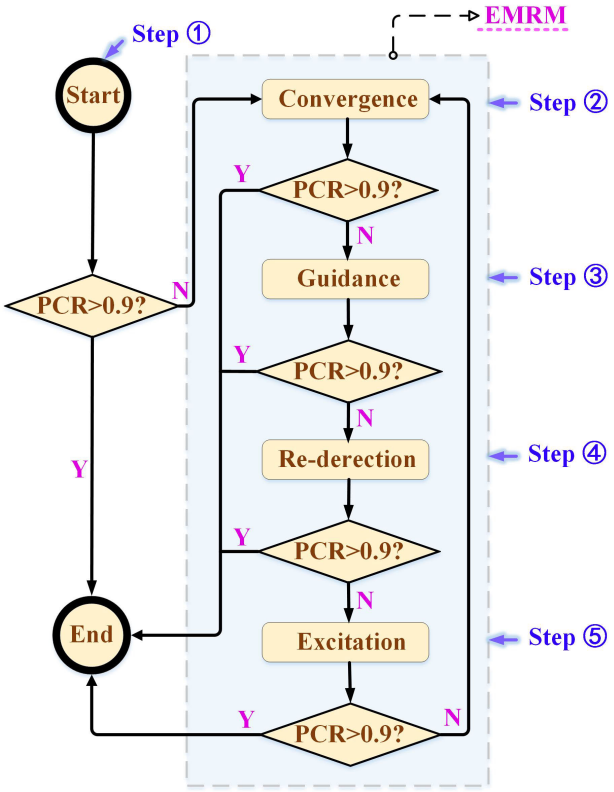

Fig. 8. Overview of the implementation process of EMRM technology.

with operating band defects, it is necessary to first assess its operational range, identify the IRFs that need to be addressed, and progressively enhance its performance using the EMRM technique. Initially, the convergence of resonant currents is achieved through the air hole-column structures to strengthen the localized field, concentrate, and relatively enhance the EMW energy involved in polarization conversion resonances. Subsequently, appropriate hole-column structures are introduced within the top-layer resonant patches to guide the currents into the main resonant region for participation in resonance. Then, based on the principle of polarization conversion, a symmetrical adjustment of the hole-column structures in the diagonal direction is performed to redirect the resonant currents and correct their directional orientation. As known, structures symmetric along the u- or v-axis direction are more conducive to achieving efficient polarization conversion effects. Finally, a narrow slit structure is constructed along the u- or v-axis direction to induce a large number of new resonant currents, making constructive contributions to optimizing the IRFs. After each iteration of the aforementioned operations, the MS is reevaluated, and if its performance has already reached the design objectives, further optimization processes are terminated.

Based on the preceding analysis, the proposed lattice unit exhibits a specific response in accordance with the implementation principle of the EMRM technique. When the EM wave impinges upon the MS, copious currents are induced in the metal resonant patches and metal reflective plate. The resonance of the effective surface current is pivotal in generating the polarization conversion effect. Fig. 9 displays the surface current modification of four IRFs under the EMRM technology. Step ② enhances the 1.11 THz IRF centrally, as depicted in Fig. 9(a), and the current direction is denoted by the red arrows. In Step ①, the currents on the resonant patch flow along the u-axis, whereas those in the metal reflective plate flow along the $-y$-axis, accompanied by weaker energy. Upon examining Step ②, it can be observed that the current in the reflective plate is focused and reinforced by the "hole-column frame." Meanwhile, the flow direction remains opposite to the strong currents in the resonant patches. Thus, a circulation is established in the dielectric layer, and according to the right-hand rule, a corresponding magnetic dipole $\boldsymbol{m}$ is induced. The corresponding magnetic field direction is oriented along the $-v$-axis and can be decomposed into $\boldsymbol{H}_x$ and $\boldsymbol{H}_y$, where the magnetic field component parallel to the electric field direction can bring about polarization conversion.

For the 1.49 THz IRF in Step ②, the addition of inner "hole-column corners" yields a positive impact, as demonstrated in Fig. 9(b). In comparison with the metal reflector, it is

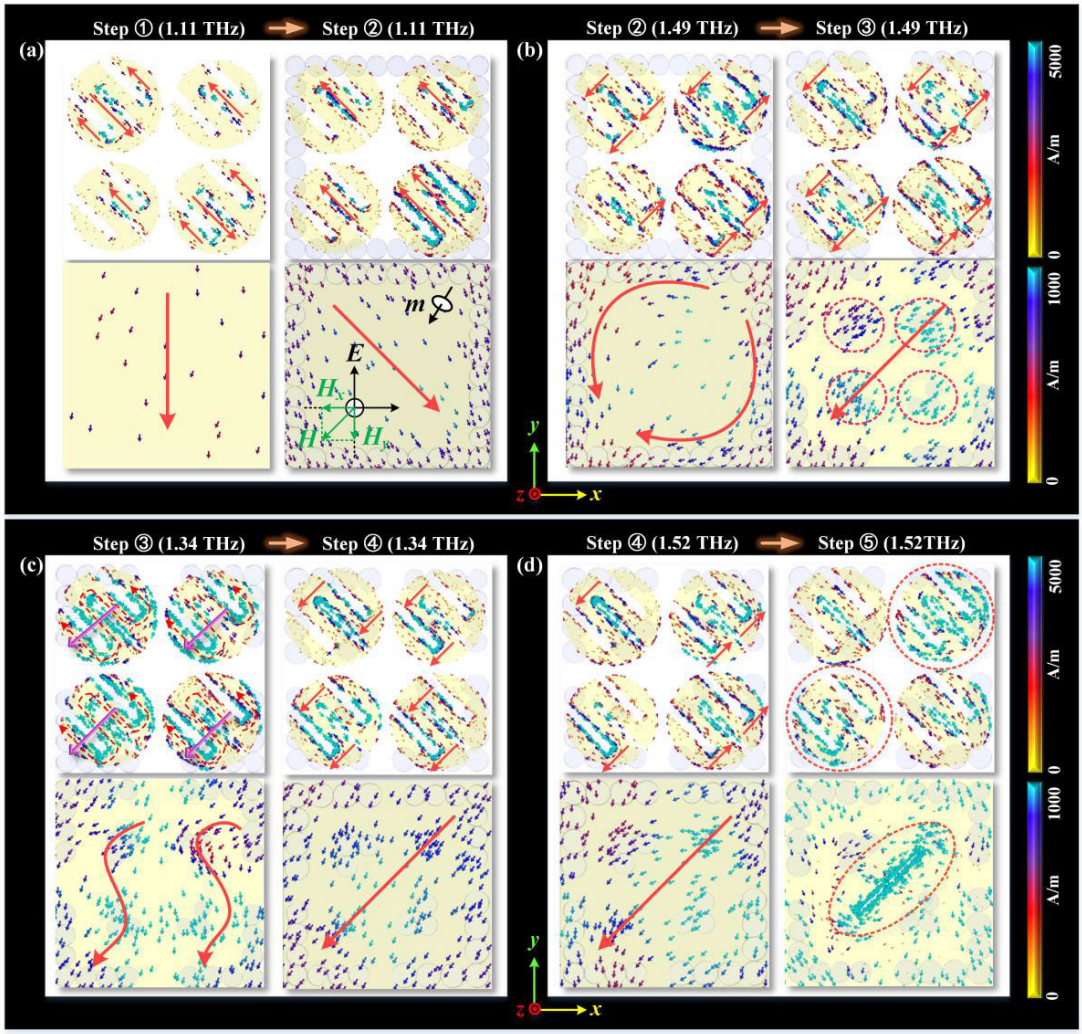

Fig. 9. Surface current distributions of (a) Step ① and Step ② at 1.11 THz, (b) Step ② and Step ③ at 1.49 THz, (c) Step ③ and Step ④ at 1.34 THz, and (d) Step ④ and Step ⑤ at 1.52 THz on metal resonant patches and metal reflector.

discernible that the currents in Step ② are low in density, insufficient in intensity, and deficient in directivity in the central major resonance region, leading to insufficient currents satisfying the resonant conditions; however, in Step ③, guided by the inner "hole-column corners," the current density and intensity escalate, with the currents flowing toward the central resonant region. Surface currents, whose directivities are rectified in the metal reflector, work in concert with the strong currents at slotted terminals of the resonant patches, engendering the corresponding magnetic resonance and electrical resonance (the specific principle is analogous to the above, so no repetition is necessary), thereby accomplishing the enhancement of polarization conversion performance.

At a frequency of 1.34 THz [as depicted in Fig. 9(c)], during both Step ③ and Step ④, the surface currents in the metal resonator and reflective plate remain oriented in the same direction, thereby inducing the polarization conversion effect mainly through electric resonance. Step ④, which involves the selection of the appropriate position and size of hole columns, serves to further rectify the current direction on the reflective plate in order to enhance influential currents. As previously mentioned, Step ④, however, demonstrates a PCR of 0.86 at 1.52 THz, indicating a significant polarization conversion effect. The directivity of the existing surface current has been reasonably satisfied, and therefore, increasing the density and intensity of the current serves as an effective strategy for improving the IRF.

As illustrated in Fig. 9(d), EMRM technology generates extensive resonant currents with significant energy in the central resonant region of the metal reflective plate via the slit structure. Simultaneously, intense currents are induced in the resonant patches located in quadrants I and II, which can be directly observed through the color change in the red dotted box. The intense resonance generated by the high current density and current intensity leads to a constructive improvement of the PCR. In conclusion, it is concluded that the EMRM technique can stimulate and induce more effective surface currents for resonance by correcting directional defects, density defects, and strength defects of the surface current distribution in the IRFs. Although further studies are necessary to confirm the origin of this intriguing phenomenon, the simulation results clearly demonstrate that the powerful polarization conversion induced by resonance plays a significant role in enhancing the IRFs in this process. Ultimately, the defective band can be

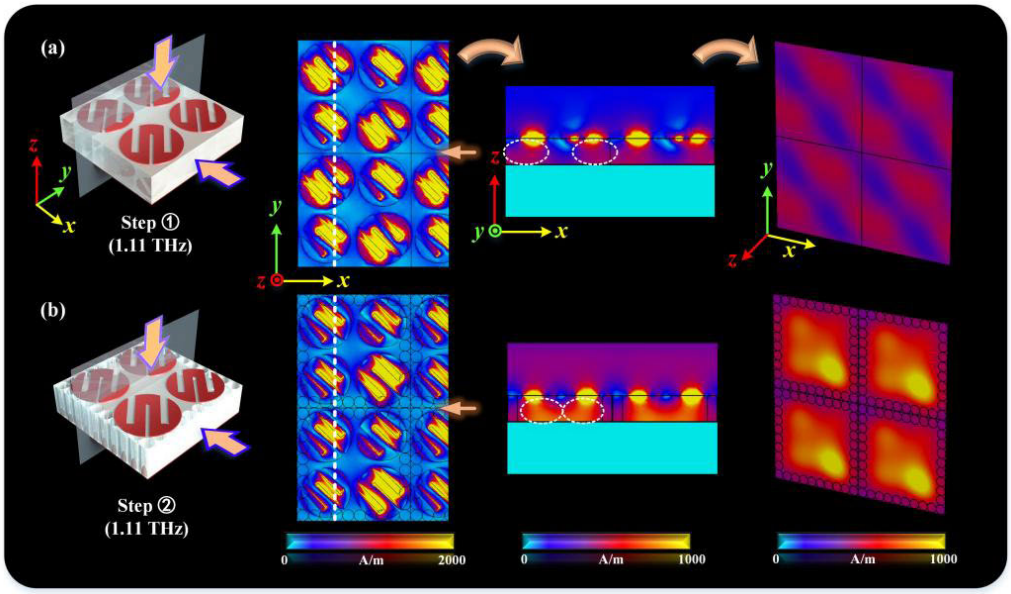

Fig. 10. Magnetic field energy distribution cross section of (a) Step ① and (b) Step ② at 1.11 THz.

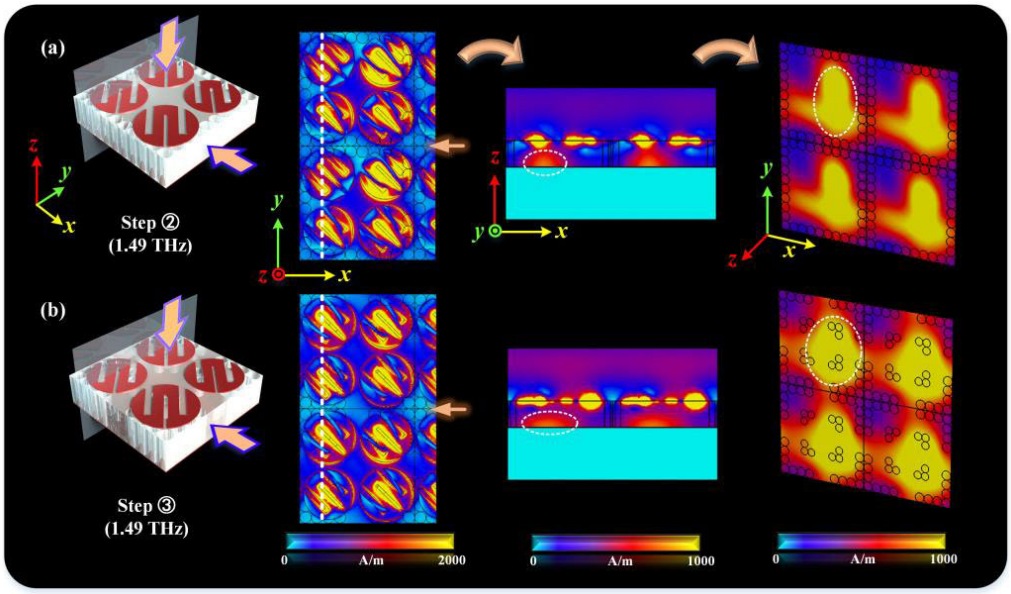

Fig. 11. Magnetic field energy distribution cross section of (a) Step ② and (b) Step ③ at 1.49 THz.

improved, leading to the realization of an ultrawideband and high-efficiency MS.

The energy distributions of the electric field and magnetic field, presented in Figs. 10–13, are used to support the aforementioned current analysis. The MS is observed from the $y0z$ and $x0y$ sections, respectively. The original point is set at the upper surface center of the dielectric substrate in the lattice unit. The $x0y$ section is uniformly selected at $z = +0.2$ μm and $z = -29$ μm to profile the resonant patch and reflective plate, respectively. At 1.11 THz IRF, the magnetic field energy distributions of Step ① and Step ② are illustrated in Fig. 10(a) and (b). In Step ①, the magnetic field exhibits robust energy at the resonant patch, while it is weak in the reflective plate, especially in quadrants II and IV. The addition of the "hole-column frame" greatly enhances and concentrates the magnetic field intensity in the metal reflection plate. The quadrant IV displays the relatively strongest energy state. The constructive advantage of the above phenomenon can be observed in the $y0z$ cross-section view (the cross-section position is arbitrarily selected, marked by the virtual white line in the figures, $x = -20$ μm in this state). The magnetic field energy in the dielectric substrate converges and increases significantly, from 470 A/m to approximately 800 A/m. This observation confirms the content presented in Fig. 9(a): the correction current enhances magnetic resonance.

In Fig. 11, a comparable situation is presented for the 1.49 THz IRF, wherein a significant modification in the

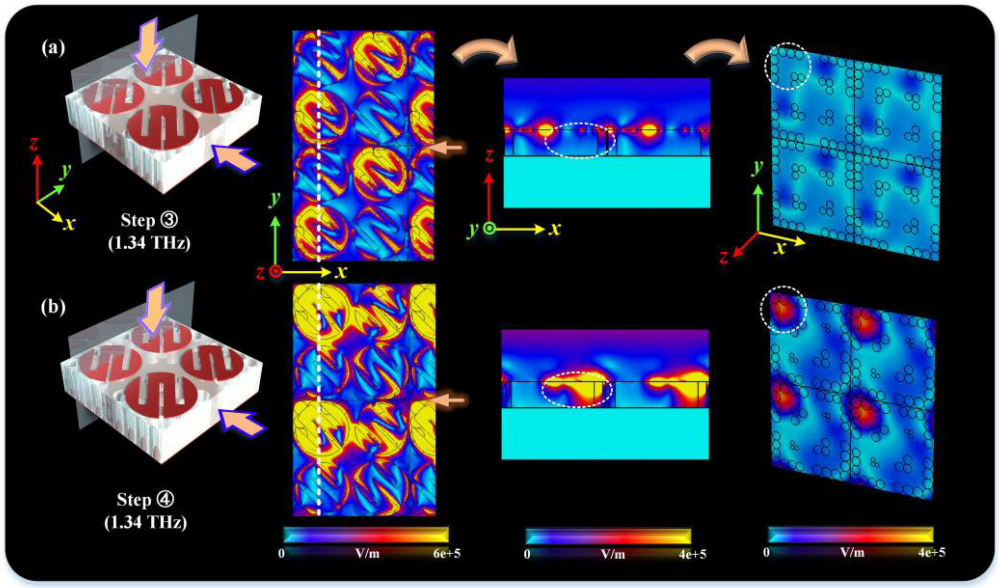

Fig. 12. Electric field energy distribution cross section of (a) Step ③ and (b) Step ④ at 1.34 THz.

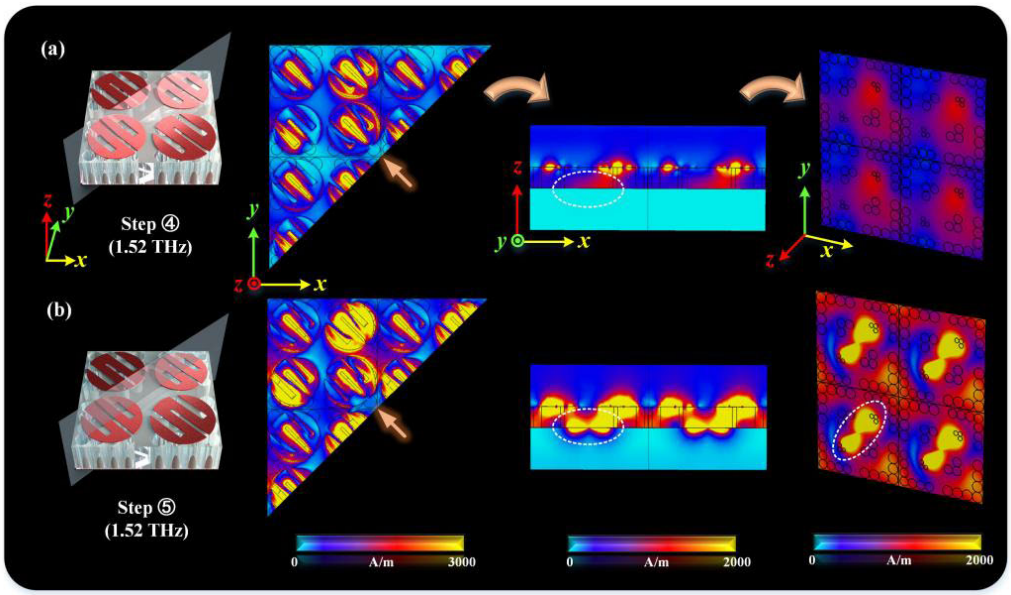

Fig. 13. Magnetic field energy distribution cross section of (a) Step ④ and (b) Step ⑤ at 1.52 THz.

magnetic field is observed on the metal reflective plate. The location with a strong magnetic field energy remained unchanged (in quadrants I and IV), but the range of its influence is notably expanded. This observation reaffirms the effectiveness of the EMRM technology in altering currents, thereby enhancing magnetic resonance. At the 1.34 THz IRF for Step ③ and Step ④, electric resonance dominates. Upon examining the energy distribution of the electric field, it is evident that the depth and intensity of resonance are substantially amplified in quadrant II. The incorporation of a slit structure along the v-axis direction on the metal reflective plate induces a substantial current, as mentioned earlier, which participates in the resonance. As a result, at 1.52 THz, the magnetic field intensity surrounding the slit displays a high numerical state, which radiates to the top resonant patches, as depicted in Fig. 13.

Furthermore, for providing additional details, relevant data and further supporting the content of the EMRM technology, the information regarding angle stability (i.e., Section I) and the effects of significant parameter variations on MS (i.e., Section II), and processing method for MS based on EMRM technology (i.e., Section III) can be found in the supplementary materials.

Table III presents a systematic summary and comparison of existing optimization methods for improving the polarization conversion performance. Initially, polarization conversion MSs primarily used fixed metal patch structures as primary resonators. With further research, the design

TABLE III
COMPARISON OF RELATED RESEARCHES FOCUSED ON THE TECHNIQUES AND METHODS FOR IMPROVING POLARIZATION CONVERSION PERFORMANCE (SIMULATION EXPERIMENTAL RESULTS)

Work	Before		After		Method
	Operating Band	Relative bandwidth	Operating Band	Relative bandwidth	
[43]	1.13~1.82 THz	46.8%	0.63~1.50 THz	81.7%	Multi-layer structure
[44]	0.93~1.05 THz	12.1%	0.76~1.12 THz	38.3%	
[45]	1.02~1.61 THz (unit C)	44.8%	0.91~1.67 THz	58.9%	Splicing technology
[46]	0.73~1.01 THz 1.23~1.42 THz	32.2% 14.3%	0.90~1.86 THz	69.6%	Air Through-hole structures
[47]	21.00~26.89 THz	24.6%	21.28~27.58 THz	25.8%	Code
This paper	0.60~0.87 THz 1.12~1.16 THz 1.20~1.29 THz	36.7% 3.5% 7.2%	0.70~1.52 THz	73.9%	EMRM technology

approach combining unique materials and metals has become widespread [40], [41], [42]; however, most optimization methods for reflective polarization conversion MSs are limited to changing the parameters of the top resonant patches. The finite parameters resulting from structural constraints impose an upper limit on performance improvements. To address this limitation, novel optimization technologies have emerged. For example, Huang et al. [44] expanded the working band by stacking multiple layers. The optimization concept of stacking multiple resonant structures relies primarily on the excitation of different interlayer resonant circulations, leading to the superposition of resonant frequencies. Multilayer designs, however, result in a large cross section of the MS, which can be detrimental to miniaturization and flat integration of the device. The splicing technique proposed by Zhang et al. [45] is conducive to band expansion and is optimized by implementing phase compensation; however, the application of splicing technology is limited to independent structures with broadband characteristics, and its initial conditions are demanding, with a weak effect on band expansion. In addition, Khajeh et al. [47] used randomly initialized hill climbing and genetic algorithms to expand the band of the polarization converter. Nevertheless, the coding for the optimal configuration is still complex and random.

Furthermore, there are several optimization techniques available for MS, such as machine learning [48], [49], transfer learning [50], and genetic algorithms [51], among others. These methods have been extensively studied and applied in the field of MS optimization, which are not further elaborated upon herein. In this study, we present a novel solution to improve polarization conversion performance while avoiding the limitations of previous designs. Through comparison with existing optimization methods in Table III, it is evident that the EMRM technology is more targeted and exhibits a higher degree of optimization. Our approach involves locally resetting and inducing surface currents in the metal reflective plate to achieve auxiliary excitation of the defect resonance region, resulting in improved PCR. This scheme uses the flexibility of the hole column in positioning, radius, and number and is complemented by the introduction of the slit structure. Through the equivalent circuit model and other demonstration methods, it is evident that the local resonance improvement induced by the EMRM technique is widely applicable to most polarization conversion MSs. Hence, this technology presents a robust platform for designing ultrawideband high-efficiency polarization conversion MS.

III. CONCLUSION

We present a comprehensive theoretical investigation model that demonstrates the implementation process of the EMRM technology. We emphasize the general applicability of this technology to most defective polarization conversion MSs. The underlying concept of EMRM technology is to enhance PCR at IRFs within the defective frequency band with a broadband effect. The preconditions for EMRM technology are established through appropriate hole-column and slit structures. Remarkably, the EMRM technology can impact and improve the depth and range of EM resonance by resetting the defect currents in the metal reflective plate. In addition to unveiling a universal technique for enhancing PCR to extend the operating band, our proposed study offers a complete solution for ultrawideband and efficient polarization conversion MS design.

REFERENCES

[1] A. Namai et al., "Synthesis of an electromagnetic wave absorber for high-speed wireless communication," *J. Amer. Chem. Soc.*, vol. 131, no. 3, pp. 1170–1173, Jan. 2009.
[2] P. Mehrotra, B. Chatterjee, and S. Sen, "EM-wave biosensors: A review of RF, microwave, mm-wave and optical sensing," *Sensors*, vol. 19, no. 5, p. 1013, Feb. 2019.

[3] F. Meng et al., "Graphene-based microwave absorbing composites: A review and prospective," *Compos. B, Eng.*, vol. 137, pp. 260–277, Mar. 2018.

[4] L.-H. Gao et al., "Broadband diffusion of terahertz waves by multi-bit coding metasurfaces," *Light, Sci. Appl.*, vol. 4, no. 9, p. e324, Sep. 2015.

[5] N. K. Grady et al., "Terahertz metamaterials for linear polarization conversion and anomalous refraction," *Science*, vol. 340, no. 6138, pp. 1304–1307, Jun. 2013.

[6] T. Kan et al., "Enantiomeric switching of chiral metamaterial for terahertz polarization modulation employing vertically deformable MEMS spirals," *Nature Commun.*, vol. 6, no. 1, p. 8422, Oct. 2015.

[7] M. J. Fitch and R. Osiander, "Terahertz waves for communications and sensing," *Johns Hopkins APL Tech. Dig.*, vol. 25, no. 4, pp. 348–355, 2004.

[8] C. Guo, F. Liu, S. Chen, C. Feng, and Z. Zeng, "Advances on exploiting polarization in wireless communications: Channels, technologies, and applications," *IEEE Commun. Surveys Tuts.*, vol. 19, no. 1, pp. 125–166, 1st Quart., 2017.

[9] Z. Shi et al., "Continuous angle-tunable birefringence with freeform metasurfaces for arbitrary polarization conversion," *Sci. Adv.*, vol. 6, no. 23, Jun. 2020, Art. no. eaba3367.

[10] S. Chen, Y. Zhang, Z. Li, H. Cheng, and J. Tian, "Empowered layer effects and prominent properties in few-layer metasurfaces," *Adv. Opt. Mater.*, vol. 7, no. 14, Jul. 2019, Art. no. 1801477.

[11] A. Kolanowska, D. Janas, A. P. Herman, R. G. Jędrysiak, T. Giżewski, and S. Bonce, "From blackness to invisibility—Carbon nanotubes role in the attenuation of and shielding from radio waves for *stealth* technology," *Carbon*, vol. 126, pp. 31–52, Jan. 2018.

[12] D. R. Smith, J. B. Pendry, and M. C. K. Wiltshire, "Metamaterials and negative refractive index," *Science*, vol. 305, no. 5685, pp. 788–792, 2004.

[13] J. B. Pendry, "Negative refraction makes a perfect lens," *Phys. Rev. Lett.*, vol. 85, no. 18, pp. 3966–3969, Oct. 2000.

[14] K. Aydin, I. Bulu, and E. Ozbay, "Subwavelength resolution with a negative-index metamaterial superlens," *Appl. Phys. Lett.*, vol. 90, no. 25, Jun. 2007, Art. no. 254102.

[15] G. Z. Zhao, S. Bi, M. Niu, and Y. Cui, "A zero refraction metamaterial and its application in electromagnetic stealth cloak," *Mater. Today Common.*, vol. 21, Dec. 2019, Art. no. 100603.

[16] D. Penninckx and V. Morénas, "Jones matrix of polarization mode dispersion," *Opt. Lett.*, vol. 24, no. 13, pp. 875–877, 1999.

[17] S. Ghosh, S. Bhattacharyya, Y. Kaiprath, and K. Vaibhav Srivastava, "Bandwidth-enhanced polarization-insensitive microwave metamaterial absorber and its equivalent circuit model," *J. Appl. Phys.*, vol. 115, no. 10, Mar. 2014, Art. no. 104503.

[18] W. H. Mcmaster, "Polarization and the Stokes parameters," *Amer. J. Phys.*, vol. 22, no. 6, pp. 351–362, Sep. 1954.

[19] P. Xie, G. Wang, H. Li, J. Liang, and X. Gao, "Circularly polarized Fabry-Pérot antenna employing a receiver–transmitter polarization conversion metasurface," *IEEE Trans. Antennas Propag.*, vol. 68, no. 4, pp. 3213–3218, Apr. 2020.

[20] X. Gao, X. Han, W.-P. Cao, H. O. Li, H. F. Ma, and T. J. Cui, "Ultrawideband and high-efficiency linear polarization converter based on double V-shaped metasurface," *IEEE Trans. Antennas Propag.*, vol. 63, no. 8, pp. 3522–3530, Aug. 2015.

[21] Y. Ji, Y. Wu, S. Guan, and X. Zhao, "3D numerical modeling of induced-polarization electromagnetic response based on the finite-difference time-domain method," *Geophysics*, vol. 83, no. 6, pp. E385–E398, Nov. 2018.

[22] D. Correia, J. P. da Silva, and H. E. Hernandez-Figueroa, "Genetic algorithm and finite-element design of short single-section passive polarization converter," *IEEE Photon. Technol. Lett.*, vol. 15, no. 7, pp. 915–917, Jun. 25, 2003.

[23] S. J. Elston, G. P. Bryan-Brown, and J. R. Sambles, "Polarization conversion from diffraction gratings," *Phys. Rev. B, Condens. Matter*, vol. 44, no. 12, pp. 6393–6400, Sep. 1991.

[24] N. Maccaferri et al., "Resonant enhancement of magneto-optical activity induced by surface plasmon polariton modes coupling in 2D magnetoplasmonic crystals," *ACS Photon.*, vol. 2, no. 12, pp. 1769–1779, Dec. 2015.

[25] J. Wang and W. Wu, "Cavity-based linear-to-circular polarization converter," *Opt. Exp.*, vol. 25, no. 4, pp. 3805–3810, 2017.

[26] H. Zhang, X. He, D. Zhang, and H. Zhang, "Multitasking device with switchable and tailored functions of ultra-broadband absorption and polarization conversion," *Opt. Exp.*, vol. 30, no. 13, pp. 23341–23358, 2022.

[27] X.-C. Zhu et al., "A novel reflective surface with polarization rotation characteristic," *IEEE Antennas Wireless Propag. Lett.*, vol. 12, pp. 968–971, 2013.

[28] M. Amiri, M. Abolhasan, N. Shariati, and J. Lipman, "Soil moisture remote sensing using SIW cavity based metamaterial perfect absorber," *Sci. Rep.*, vol. 11, no. 1, pp. 1–17, Mar. 2021.

[29] T. T. Lv et al., "Hybrid metamaterial switching for manipulating chirality based on VO2 phase transition," *Sci. Rep.*, vol. 6, no. 1, pp. 1–9, Mar. 2016.

[30] H. F. Zhang, G. B. Liu, T. Huang, and L. Zeng, "Design of a frequency reconfigurable broadband THz antenna based on the vanadium dioxide," *Plasmonics*, vol. 15, pp. 1035–1041, Jan. 2020.

[31] W. Chen, C. A. Balanis, and C. R. Birtcher, "Checkerboard EBG surfaces for wideband radar cross section reduction," *IEEE Trans. Antennas Propag.*, vol. 63, no. 6, pp. 2636–2645, Jun. 2015.

[32] W.-L. Guo et al., "Broadband polarization-conversion metasurface for a Cassegrain antenna with high polarization purity," *Phys. Rev. Appl.*, vol. 12, no. 1, Jul. 2019, Art. no. 014009.

[33] R. T. Ako, A. Upadhyay, W. Withayachumnankul, M. Bhaskaran, and S. Sriram, "Dielectrics for terahertz metasurfaces: Material selection and fabrication techniques," *Adv. Opt. Mater.*, vol. 8, no. 3, Feb. 2020, Art. no. 1900750.

[34] P. Xu, W. X. Jiang, S. Y. Wang, and T. J. Cui, "An ultrathin cross-polarization converter with near unity efficiency for transmitted waves," *IEEE Trans. Antennas Propag.*, vol. 66, no. 8, pp. 4370–4373, Aug. 2018.

[35] Y. Li and B. M. Assouar, "Acoustic metasurface-based perfect absorber with deep subwavelength thickness," *Appl. Phys. Lett.*, vol. 108, no. 6, Feb. 2016, Art. no. 063502.

[36] D.-Y. Maa, "Potential of microperforated panel absorber," *J. Acoust. Soc. Amer.*, vol. 104, no. 5, pp. 2861–2866, Nov. 1998.

[37] X. Gao, W. L. Yang, H. F. Ma, Q. Cheng, X. H. Yu, and T. J. Cui, "A reconfigurable broadband polarization converter based on an active metasurface," *IEEE Trans. Antennas Propag.*, vol. 66, no. 11, pp. 6086–6095, Nov. 2018.

[38] J. A. H. van Nieuwstadt et al., "Strong modification of the nonlinear optical response of metallic subwavelength hole arrays," *Phys. Rev. Lett.*, vol. 97, no. 14, Oct. 2006, Art. no. 146102.

[39] B.-L. Wang, R. Wang, R. J. Liu, X. H. Lu, J. Zhao, and Z.-Y. Li, "Origin of shape resonance in second-harmonic generation from metallic nanohole arrays," *Sci. Rep.*, vol. 3, no. 1, pp. 1–8, Aug. 2013.

[40] Z.-G. Liu, Z.-X. Cao, and L.-N. Wu, "Compact low-profile circularly polarized Fabry–Pérot resonator antenna fed by linearly polarized microstrip patch," *IEEE Antennas Wireless Propag. Lett.*, vol. 15, pp. 524–527, 2016.

[41] O. Altintas, E. Unal, O. Akgol, M. Karaaslan, F. Karadag, and C. Sabah, "Design of a wide band metasurface as a linear to circular polarization converter," *Modern Phys. Lett. B*, vol. 31, no. 30, Oct. 2017, Art. no. 1750274.

[42] L. Liu et al., "Broadband metasurfaces with simultaneous control of phase and amplitude," *Adv. Mater.*, vol. 26, no. 29, pp. 5031–5036, Aug. 2014.

[43] Y. P. Li, H. F. Zhang, T. Yang, T. Y. Sun, and L. Zeng, "Realizing ultra-bandwidth cross-polarization conversion by a double-layer metasurface," *J. Opt. Soc. Amer. B, Opt. Phys.*, vol. 37, no. 12, pp. 3572–3580, 2020.

[44] W. Huang, X. Hao, Y. Cheng, S. Yin, J. Han, and W. Zhang, "Broadband terahertz half-wave plate with multi-layered metamaterials designed via quantum engineering," *J. Lightw. Technol.*, vol. 39, no. 24, pp. 7925–7929, Dec. 15, 2021.

[45] X. L. Zhang, H. N. Ye, Y. Zhao, and H. F. Zhang, "A tunable ultra-wideband cross-polarization conversion based on the band splicing technology," *Appl. Phys. B, Lasers Opt.*, vol. 127, p. 69, Apr. 2021.

[46] Y. P. Li, L. Zeng, and H. F. Zhang, "Technique for improving polarization conversion performance," *J. Opt. Soc. Amer. B, Opt. Phys.*, vol. 39, no. 10, pp. 2573–2581, 2022.

[47] A. Khajeh, Z. Hamzavi-Zarghani, A. Yahaghi, and A. Farmani, "Tunable broadband polarization converters based on coded graphene metasurfaces," *Sci. Rep.*, vol. 11, no. 1, p. 1296, Jan. 2021.

[48] Q. Zhang et al., "Machine-learning designs of anisotropic digital coding metasurfaces," *Adv. Theory Simulations*, vol. 2, no. 2, Feb. 2019, Art. no. 1800132.

[49] L. Li et al., "Machine-learning reprogrammable metasurface imager," *Nature Commun.*, vol. 10, no. 1, p. 1082, Mar. 2019.

[50] R. Zhu et al., "Phase-to-pattern inverse design paradigm for fast realization of functional metasurfaces via transfer learning," *Nature Commun.*, vol. 12, no. 1, p. 2974, May 2021.

[51] S. Jafar-Zanjani, S. Inampudi, and H. Mosallaei, "Adaptive genetic algorithm for optical metasurfaces design," *Sci. Rep.*, vol. 8, no. 1, p. 11040, Jul. 2018.

Yu-Peng Li is currently pursuing the master's degree with the College of Electronic and Optical Engineering and the College of Flexible Electronics (Future Technology), Nanjing University of Posts and Telecommunications, Nanjing, China.

Her main research interests include metastructure-based polarization converter, absorption, and its reconfigurable and optimized methods.

Zhen Qiao was born in Jiangsu, China, in 2001. He is currently pursuing the master's degree with the Nanjing University of Posts and Telecommunications, Nanjing, China.

His main research interests include polarization converters and tunable metamaterials.

Ke Xia is currently pursuing the master's degree with the College of Electronic and Optical Engineering and the College of Flexible Electronics (Future Technology), Nanjing University of Posts and Telecommunications, Nanjing, China.

His main research interests include antenna arrays, dielectric resonators, and multipole mode theory.

Lei Zhang is currently pursuing the master's degree with the College of Electronic and Optical Engineering and the College of Flexible Electronics (Future Technology), Nanjing University of Posts and Telecommunications, Nanjing, China.

His main research interests include circularly polarized antenna arrays, reconfigurable antennas, and characteristic mode analysis.

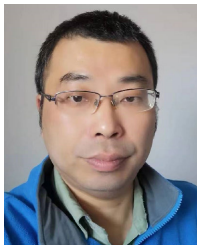

Hai-Feng Zhang received the Ph.D. degree from the College of Electronic and Information Engineering, Nanjing University of Aeronautics and Astronautics, Nanjing, China.

He is currently working as a Professor at the College of Electronic and Optical Engineering and the College of Flexible Electronics (Future Technology), Nanjing University of Posts and Telecommunications, Nanjing. His main research interests include computational electromagnetics, plasma photonic crystal, plasma stealthy, and electromagnetic properties of metamaterials.